



ATLAS NOTE

ATLAS-CONF-2016-096

1st September 2016



Search for the electroweak production of charginos and neutralinos in multilepton final states at $\sqrt{s} = 13$ TeV with the ATLAS detector

The ATLAS Collaboration

Abstract

This note reports on the searches for direct production of opposite-sign pair of the lightest charginos ($\tilde{\chi}_1^{\pm}\tilde{\chi}_1^{\mp}$) and the pair production of the lightest chargino with the next-to-the-lightest neutralino ($\tilde{\chi}_1^{\pm}\tilde{\chi}_2^0$) using 13.3 fb^{-1} of integrated luminosity from LHC pp collisions at $\sqrt{s} = 13$ TeV collected by the ATLAS detector. These studies have been performed in final states including two and three leptons (electrons or muons) and large missing transverse momentum. The results have been found to be in agreement with the Standard Model expectations. Exclusion limits at 95% confidence level are derived on the masses of the $\tilde{\chi}_1^{\pm}/\tilde{\chi}_2^0$ (assumed to be mass degenerate) and the lightest neutralino ($\tilde{\chi}_1^0$) assuming 100% branching ratio of the $\tilde{\chi}_1^{\pm}$ and $\tilde{\chi}_2^0$ to sleptons ($\tilde{\ell}$). These results extend the region of supersymmetric parameter space excluded by the Run I LHC searches. For the case of $\tilde{\chi}_1^{\pm}\tilde{\chi}_1^{\mp}$ scenario the observed limit on the $m_{\tilde{\chi}_1^{\pm}}$ is at 620 GeV while for the case of $\tilde{\chi}_1^{\pm}\tilde{\chi}_2^0$ the observed limit on $m_{\tilde{\chi}_1^{\pm}/\tilde{\chi}_2^0}$ has been extended to 1 TeV for massless $\tilde{\chi}_1^0$.

1 Introduction

Supersymmetry (SUSY) [1–7] is one of the most studied extensions to the Standard Model (SM), due to its ability to provide an elegant solution to the SM Hierarchy problem [8–11]. In its minimal realisation (the Minimal Supersymmetric Standard Model, or MSSM) [12, 13], it predicts a new bosonic (fermionic) partner for each fundamental SM fermion (boson), as well as an additional Higgs doublet. If R -parity is conserved [14] the lightest supersymmetric particle (LSP) is stable. This is typically the lightest neutralino¹ $\tilde{\chi}_1^0$, which can then provide a natural candidate for dark matter [15, 16]. If produced in the decay of heavier SUSY particles, a neutralino LSP would escape detection in ATLAS, leading to an amount of missing transverse momentum (E_T^{miss}) significantly larger than SM processes, that can be exploited to extract SUSY signals.

The production cross sections of SUSY sparticles at the LHC depend both on the type of interaction involved and on the mass of the sparticles. The coloured sparticles (squarks and gluinos) have significantly larger production cross sections (strong production) than non-coloured sparticles of equal masses such as the Electroweakinos ($\tilde{\chi}^\pm$ and $\tilde{\chi}^0$) and the sleptons ($\tilde{\ell}$ and $\tilde{\nu}$). The direct production of Electroweakinos or sleptons can dominate SUSY production at the LHC if the masses of the gluinos and squarks are significantly heavier. The current searches from the ATLAS and CMS collaborations during LHC Run II excluded gluino (squark) masses up to 1.8 TeV (1.3 TeV) [17, 18].

This note presents a search with the ATLAS detector for the direct production of charginos and neutralinos decaying to final states with two or three leptons (electrons or muons) and large missing transverse momentum. The analysis is based on 13.3 fb^{-1} of proton-proton collision data delivered by the LHC at a centre-of-mass energy of $\sqrt{s}=13 \text{ TeV}$. Similar studies have been performed during LHC Run I from both the ATLAS and CMS collaborations and have been reported in Refs [19–21] and [22, 23], respectively.

This approach is detailed in Section 6, preceded by descriptions of the experimental apparatus (Section 2), the SUSY scenarios considered (Section 3), the simulated samples (Section 4) and the object reconstruction (Section 5). Section 7 is devoted to the estimation of the contribution from SM processes to the signal regions, while Section 8 reports on the systematic uncertainties affecting the current searches. The results are presented in Section 9, together with the statistical tests used to interpret the results in the context of the SUSY benchmark scenarios. Finally, Section 10 summarises the main conclusions of this note.

2 The ATLAS detector

The ATLAS experiment [24] is a multi-purpose particle detector with a forward-backward symmetric cylindrical geometry and nearly 4π coverage in solid angle.² The interaction point is surrounded by an inner detector (ID), a calorimeter system, and a muon spectrometer.

¹ The SUSY partners of the Higgs and electroweak gauge bosons mix to form the mass eigenstates known as charginos ($\tilde{\chi}_l^\pm$, $l = 1, 2$ ordered by increasing mass) and neutralinos ($\tilde{\chi}_m^0$, $m = 1, \dots, 4$ ordered by increasing mass).

² ATLAS uses a right-handed coordinate system with its origin at the nominal interaction point (IP) in the centre of the detector and the z -axis along the beam pipe. The x -axis points from the IP to the centre of the LHC ring, and the y -axis points upward. Cylindrical coordinates (r, ϕ) are used in the transverse plane, ϕ being the azimuthal angle around the beam pipe. The pseudorapidity is defined in terms of the polar angle θ as $\eta = -\ln \tan(\theta/2)$. Rapidity is defined as $y = 0.5 \ln [(E + p_z)/(E - p_z)]$ where E denotes the energy and p_z is the component of the momentum along the beam direction.

The ID provides precision tracking of charged particles for pseudorapidities $|\eta| < 2.5$ and is surrounded by a superconducting solenoid providing a 2 T axial magnetic field. It consists of pixel and silicon-microstrip detectors inside a transition radiation tracker. One significant upgrade for the $\sqrt{s} = 13$ TeV running period is the presence of the Insertable B-Layer [25], an additional pixel layer close to the interaction point, which provides high-resolution hits at small radius to improve the tracking performance.

In the pseudorapidity region $|\eta| < 3.2$, high-granularity lead/liquid-argon (LAr) electromagnetic (EM) sampling calorimeters are used. A steel/scintillator tile calorimeter measures hadron energies for $|\eta| < 1.7$. The endcap and forward regions, spanning $1.5 < |\eta| < 4.9$, are instrumented with LAr calorimeters for both the EM and hadronic measurements.

The muon spectrometer consists of three large superconducting toroids with eight coils each, a system of trigger and precision-tracking chambers, which provide triggering and tracking capabilities in the ranges $|\eta| < 2.4$ and $|\eta| < 2.7$, respectively.

A two-level trigger system is used to select events. The first-level trigger is implemented in hardware and uses a subset of the detector information. This is followed by the software-based High-Level Trigger stage, which can run offline reconstruction and calibration software, reducing the event rate to about 1 kHz.

3 SUSY scenarios

This search targets two electroweak SUSY production processes which decay into final states containing two or three leptons, in the context of simplified models [26]. Tree-level diagrams for these processes are shown in Figure 1. The left-handed sleptons are assumed to be degenerate and have a mass $m_{\ell_L} = (m_{\tilde{\chi}_2^0} + m_{\tilde{\chi}_1^0})/2$. The masses and the decay modes of the relevant particles ($\tilde{\chi}_2^0, \tilde{\chi}_1^\pm, \tilde{\chi}_1^0, \tilde{\ell}, \tilde{\nu}$) are the only free parameters. The $\tilde{\chi}_2^0$ and/or $\tilde{\chi}_1^\pm$ are set to be wino-like and mass degenerate, and the $\tilde{\chi}_1^0$ is set to be bino-like.

The first scenario, shown in Figure 1(a), is direct $\tilde{\chi}_1^+ \tilde{\chi}_1^-$ production decaying with intermediate $\tilde{\ell}$ leading to a signature of a pair of opposite-sign (OS) leptons and E_T^{miss} , $\tilde{\chi}_1^+ \tilde{\chi}_1^- \rightarrow \tilde{\ell} \nu_\ell (\tilde{\nu} \ell) \tilde{\ell}' \nu_{\ell'} (\tilde{\nu}' \ell') \rightarrow \ell \ell' + E_T^{\text{miss}}$. The second scenario, shown in Figure 1(b), is direct $\tilde{\chi}_1^\pm \tilde{\chi}_2^0$ production decaying with intermediate $\tilde{\ell}$ into three leptons and E_T^{miss} , $\tilde{\chi}_1^\pm \tilde{\chi}_2^0 \rightarrow \tilde{\ell} \nu (\tilde{\nu} \ell) \tilde{\ell} \ell (\tilde{\nu} \nu) \rightarrow 3\ell + E_T^{\text{miss}}$.

4 Dataset and Monte Carlo simulation

This analysis uses data delivered by the LHC at 13 TeV in 2015 and 2016. After fulfilling data-quality requirements, the data sample amounts to an integrated luminosity of 13.3 fb^{-1} with an uncertainty of $\pm 2.9\%$. This preliminary uncertainty is derived using a methodology similar to that detailed in Refs. [27] and [28], from a preliminary calibration of the luminosity scale using x-y beam-separation scans performed in August 2015 and May 2016.

Various samples of Monte Carlo (MC) simulated events are used to model the SUSY signal and in the estimation of the Standard Model backgrounds. The samples include an ATLAS detector simulation [29], based on GEANT4 [30], or a fast simulation that uses a parameterisation of the calorimeter response and

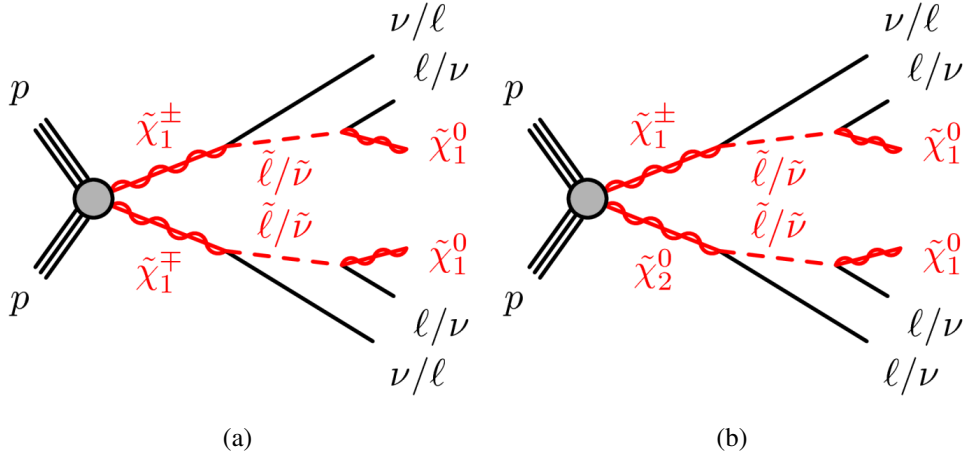


Figure 1: Diagrams for the two physics scenarios studied in this note: (a) $\tilde{\chi}_1^{\pm}\tilde{\chi}_1^-$ with $\tilde{\ell}$ -mediated decays, (b) $\tilde{\chi}_1^{\pm}\tilde{\chi}_2^0$ with $\tilde{\ell}$ -mediated decays.

GEANT4 for the other parts of the detector [31]. The simulated events are reconstructed in the same manner as the data.

SM diboson processes with four charged leptons (ℓ), three charged leptons and one neutrino, or two charged leptons and two neutrinos are simulated using the SHERPA v2.1.1 generator [32, 33]. The matrix elements contain the diboson WW , WZ and ZZ processes and all other diagrams with four or six electroweak vertices (such as same-electric-charge W boson production in association with two jets, $W^\pm W^\pm jj$).

Fully leptonic triboson processes (WWW , WWZ , WZZ and ZZZ) with up to six charged leptons are also simulated using SHERPA v2.1.1 and described in Ref. [33]. The 4ℓ and $2\ell + 2\nu$ processes are calculated at next-to-leading order (NLO) for up to one additional parton; final states with two and three additional partons are calculated at leading order (LO). The $WWZ \rightarrow 4\ell + 2\nu$ or $2\ell + 4\nu$ processes are calculated at LO with up to two additional partons. The $3\ell + 1\nu$ process is calculated at NLO and up to three extra partons at LO using the Comix [34] and OpenLoops [35] matrix element generators and merged with the SHERPA parton shower [36] using the ME+PS@NLO prescription [37]. The $WWZ/WZZ \rightarrow 3\ell + 3\nu$, $ZZZ \rightarrow 6\ell + 0\nu$, $4\ell + 2\nu$ or $2\ell + 4\nu$ processes are calculated with the same configuration but with up to only two extra partons at LO. The CT10 [38] parton distribution function (PDF) set is used for all SHERPA samples in conjunction with a dedicated tuning of the parton shower parameters developed by the SHERPA authors. The generator cross-sections (at NLO for most of the processes) are used when normalising these backgrounds.

Events containing Z bosons with associated jets ($Z/\gamma^* + \text{jets}$) are produced using the SHERPA v2.2 generator with massive b/c-quarks to improve the treatment of the associated production of Z bosons with heavy flavour jets [39]. Matrix elements are calculated for up to two partons at NLO and up to four partons at leading order (LO). The matrix elements are calculated using the COMIX and OPENLOOPS generators of matrix elements and merged with the SHERPA parton shower using the ME+PS@NLO prescription. The CT10 PDF set is used in conjunction with a dedicated parton shower tuning developed by the SHERPA authors. A global k -factor is used to normalise the $Z/\gamma^* + \text{jets}$ events to the NNLO QCD cross sections.

For the production of $t\bar{t}$ and single top-quarks in the Wt channel, the POWHEG-BOX v2 generator with the CT10 PDF set is used [40]. The top quark mass is assumed to be 172.5 GeV. The $t\bar{t}$ (single top) events

are normalised to the NNLO + NNLL QCD [41] (NLO) cross sections.

Samples of $t\bar{t}V$ (with $V = W$ and Z , including non-resonant Z/γ^* contributions) and $t\bar{t}WW$ production are generated at LO with **MADGRAPH** v2.2.2 [42] interfaced to the **PYTHIA** 8.186 [43] parton shower model, with up to two ($t\bar{t}W$), one ($t\bar{t}Z$) or no ($t\bar{t}WW$) extra partons included in the matrix element; they are described in detail in [44]. **MADGRAPH** is also used to simulate the tZ , $t\bar{t}t\bar{t}$ and $t\bar{t}t$ processes. The A14 set of tuned parameters (tune) [45] is used together with the NNPDF23LO PDF set [46]. The $t\bar{t}W$, $t\bar{t}Z$, $t\bar{t}WW$ and $t\bar{t}t\bar{t}$ events are normalised to their NLO cross-section [47] while the generator cross-section is used for tZ and $t\bar{t}t$.

The signal SUSY processes are generated from LO matrix elements with up to two extra partons, using the **MADGRAPH** v2.2.3 generator interfaced to **PYTHIA** 8.186 with the A14 tune for the modelling of the SUSY decay chain, parton showering, hadronisation and the description of the underlying event. Parton luminosities are provided by the NNPDF23LO PDF set. Jet–parton matching is realised following the CKKW-L prescription [48], with a matching scale set to one quarter of the pair-produced superpartner mass. Signal cross-sections are calculated to NLO in the strong coupling constant, adding the resummation of soft gluon emission at next-to-leading-logarithmic accuracy (NLO+NLL) [49–53]. The nominal cross-section and the uncertainty are taken from an envelope of cross-section predictions using different PDF sets and factorisation and renormalisation scales, as described in Ref. [54]. The production cross-section of $\tilde{\chi}_1^{\pm}\tilde{\chi}_1^{\mp}$ with a mass of 600 GeV is 9.50 fb at $\sqrt{s} = 13$ TeV (compared with 1.96 fb at $\sqrt{s} = 8$ TeV), while the production cross-section of pairs of $\tilde{\chi}_1^{\pm}\tilde{\chi}_2^0$ with a mass of 800 GeV is 4.76 fb at $\sqrt{s} = 13$ TeV (compared with 0.68 fb at $\sqrt{s} = 8$ TeV).

In all MC samples, except those produced by **SHERPA**, the **EVTGEN** v1.2.0 program [55] is used to model the properties of the bottom and charm hadron decays. To simulate the effects of additional pp collisions in the same and nearby bunch crossings, additional interactions are generated using the soft QCD processes of **PYTHIA** 8.186 with the A2 tune [56] and the MSTW2008LO PDF set [57], and overlaid onto the simulated hard scatter event. The Monte Carlo samples are reweighted so that the distribution of the number of reconstructed vertices matches the distribution observed in the data.

5 Event reconstruction and pre-selection

Events recorded during stable data-taking conditions are used in the analysis if the reconstructed primary vertex [58] has at least two tracks with transverse momentum $p_T > 400$ MeV associated with it. The primary vertex of an event is identified as the vertex with the highest Σp_T^2 of associated tracks.

Two identification criteria are defined for the objects used in these analyses, these are named as “baseline” and “signal” (with the “signal” objects being a subset of the baseline ones). The former is defined in order to perform data-driven non-prompt leptonic background estimates (discussed in Section 7) while the latter is used when defining regions where SUSY signal is enhanced.

Electron candidates are reconstructed from an isolated electromagnetic calorimeter energy deposit matched to an ID track and are required to have $|\eta| < 2.47$, a transverse momentum $p_T > 10$ GeV, and to pass a loose likelihood-based identification requirement [59, 60]. The likelihood input variables include measurements of calorimeter shower shapes and track properties from the ID.

Muon candidates are reconstructed in the region $|\eta| < 2.5$ from muon spectrometer tracks matching ID tracks. All muons must have $p_T > 10$ GeV and must pass the medium identification requirements

defined in Ref. [61], based on selections on the number of hits in the different ID and muon spectrometer subsystems, and the significance of the charge to momentum ratio q/p [61].

Jets are reconstructed with the anti- k_t algorithm [62] with radius parameter $R = 0.4$, using three-dimensional energy clusters in the calorimeter [63] as input. All jets must have $p_T > 20\text{ GeV}$ and $|\eta| < 2.8$. Jets are calibrated as described in Ref. [64]. In order to reduce the effects of pileup, for jets with $p_T < 60\text{ GeV}$ and $|\eta| < 2.4$ a significant fraction of the tracks associated with each jet must have an origin compatible with the primary vertex, as defined by the jet vertex tagger [65]. Furthermore, for all jets the expected average energy contribution from pileup clusters is subtracted according to the jet area [64].

Identification of jets containing b -hadrons (b -tagging) is performed with the MV2c10 algorithm, a multivariate discriminant making use of track impact parameters and reconstructed secondary vertices [66, 67]. A requirement is chosen corresponding to a 77% average efficiency obtained for b -jets in simulated $t\bar{t}$ events.

After object identification, an “object-removal procedure” is performed on all candidate objects to remove possible double-counting in the reconstruction:

1. Any electron sharing an ID track with a muon is removed.
2. Jets within $\Delta R = \sqrt{(\Delta y)^2 + (\Delta\phi)^2} = 0.2$ of an electron candidate are discarded. These mostly originate from calorimeter energy deposits from electron shower.
3. Electrons within $\Delta R = 0.4$ of a jet candidate are discarded, to suppress electrons from semileptonic decays of c - and b -hadrons.
4. Jets with fewer than three associated tracks or with a nearby muon with a significant fraction of the jet p_T ($p_T^\mu > 0.5 p_T^{\text{jet}}$ and $p_T^\mu > 0.7 \sum p_T^{\text{jet tracks}}$, where p_T^μ , p_T^{jet} and $p_T^{\text{jet tracks}}$ are the p_T of the muon, jet and jet tracks, respectively) are discarded either if the candidate muon is within $\Delta R = 0.2$ or if the muon can be matched to a track associated with the jet.
5. Muons within $\Delta R = 0.4$ of a jet candidate are discarded to suppress muons from semileptonic decays of c - and b -hadrons.

Signal electrons must satisfy a medium likelihood-based identification requirement [59, 60] and the track associated with the electron must have a significance of the transverse impact parameter with respect to the reconstructed primary vertex, d_0 , of $|d_0|/\sigma(d_0) < 5$, with $\sigma(d_0)$ being the uncertainty on d_0 . In addition, the longitudinal impact parameter (again with respect to the reconstructed primary vertex), z_0 , must satisfy $|z_0 \sin \theta| < 0.5\text{ mm}$. Similarly, signal muons must satisfy the requirements of $|d_0|/\sigma(d_0) < 3$ and $|z_0 \sin \theta| < 0.5\text{ mm}$. Isolation requirements are also applied to both the signal electrons and muons.

The E_T^{miss} is defined as the magnitude of the two-dimensional vector, $\mathbf{p}_T^{\text{miss}}$, which is the negative vector sum of the transverse momenta of all identified physics objects (electrons, photons, muons, jets) and an additional soft term. The soft term is constructed from all tracks that are not associated with any physics object, and which are associated with the primary vertex. The E_T^{miss} is adjusted for the best calibration of the jets and the other identified physics objects above, while maintaining pileup independence in the soft term [68, 69].

Events are accepted if they pass an online (trigger) selection requiring either two electrons, two muons or an electron plus a muon. The trigger-level requirements on the p_T of the leptons involved in the trigger decision (the p_T thresholds range between 8–22 GeV) are looser than those applied offline to ensure that trigger efficiencies are constant in the relevant phase space. Events are discarded if they contain any jet failing basic quality selection criteria that reject detector noise and non-collision backgrounds [70].

Simulated events are corrected to account for minor differences in the signal lepton trigger, reconstruction, identification and isolation efficiencies between data and MC simulation.

6 Signal region selection

This section presents the signal region (SR) definitions, designed to search for $\tilde{\chi}_1^{\pm}\tilde{\chi}_1^{\mp}$ in two-lepton final states and for $\tilde{\chi}_1^{\pm}\tilde{\chi}_2^0$ in three-lepton final states.

6.1 Two-lepton analysis

For the two-lepton search, events are selected if they contain exactly two OS baseline leptons (e/μ) which pass the signal requirements. The p_T of the leading and sub-leading lepton are required to exceed 25 GeV and 20 GeV respectively, to ensure that the events are above the turn-on region of the di-lepton triggers. Events are divided into two channels; the “same flavour” (SF) channel contains di-electron (e^+e^-) and di-muon ($\mu^+\mu^-$) events and the “different flavour” (DF) selects electron-muon ($e^+\mu^-$, $e^-\mu^+$) events. In the SF channel, the signal regions include a “Z-veto” to reduce the contribution from the Z +jets background, where the invariant mass of the SF OS pair must satisfy $|m_{\text{SFOS}} - m_Z| > 10$ GeV. Events entering the signal regions must also satisfy a jet-veto. Events passing the jet veto must contain no jets in any of the three orthogonal categories:

1. Central light jets: $p_T > 20(30)$ GeV in the SF (DF) channel, $|\eta| < 2.4$ and not b -tagged (77% WP).
2. Central b -tagged jets: $p_T > 20$ GeV, $|\eta| < 2.4$ and b -tagged (77% WP).
3. Forward jets: $p_T > 30$ GeV, $2.4 < |\eta| < 4.5$.

These jet categories are also used when defining control regions (CRs) to determine the normalisation of the diboson background in Section 7. In order to suppress further the contributions from the SM process, the two-lepton search makes use of the “stransverse” mass, m_{T2} [71, 72], defined as

$$m_{\text{T2}} = \min_{\mathbf{q}_T} \left[\max \left(m_T(\mathbf{p}_T^{\ell 1}, \mathbf{q}_T), m_T(\mathbf{p}_T^{\ell 2}, \mathbf{p}_T^{\text{miss}} - \mathbf{q}_T) \right) \right],$$

where $\mathbf{p}_T^{\ell 1}$ and $\mathbf{p}_T^{\ell 2}$ are the transverse momenta of the two leptons, and \mathbf{q}_T is a transverse vector that minimizes the larger of the two transverse masses m_T . The latter is defined by

$$m_T(\mathbf{p}_T, \mathbf{q}_T) = \sqrt{2(p_T q_T - \mathbf{p}_T \cdot \mathbf{q}_T)}.$$

Three signal regions are defined with cuts on m_{T2} at 90 GeV, 120 GeV and 150 GeV, respectively referred to as SR2 ℓ -A, B, and C throughout this document. The tighter requirements on m_{T2} give more sensitivity to models with large mass differences between the chargino and the LSP, whereas the lower cut has more sensitivity to smaller mass splittings. This is due to the dependence of the kinematic endpoint of the m_{T2} distribution on the mass splittings between the sparticles.

The selection criteria defining the two-lepton signal regions are summarized in the Table 1. The convention 0_X is introduced where “X” (in units of GeV) indicates the p_T cut on the jet that is being vetoed.

Variable	SR2 ℓ	
lepton	$\ell^+ \ell^-$	
lepton flavour	SF	DF
central light jets	0 ₂₀	0 ₃₀
central b -jets	0 ₂₀	0 ₂₀
forward jets	0 ₃₀	0 ₃₀
$ m_{\ell\ell} - m_Z $ [GeV]	> 10	–
m_{T2} [GeV]	> 90, 120, 150	

Table 1: Signal region definitions for the 2L OS analysis. Units of the subscripts of the jet numbers are in GeV.

6.2 Three-lepton analysis

For the three-lepton search, events are selected by requiring exactly three baseline leptons satisfying the signal lepton requirements and the two of them must form a SF OS pair (as expected in $\tilde{\chi}_2^0 \rightarrow \ell^+ \ell^- \tilde{\chi}_1^0$ decays). The ambiguities, in the case where multiple SF OS pairs are present in the event, are resolved by selecting the pair candidate with an invariant mass closest to that of the Z boson. The main discriminating variables used correspond to the transverse mass, the transverse momentum of the third leading lepton and E_T^{miss} . Similar to the two-lepton selections, a b -tag jet veto (with the same p_T threshold) is required for suppressing the contributions from processes containing b -quark. Both signal regions target large mass differences between the $\tilde{\chi}_1^\pm/\tilde{\chi}_2^0$ and the LSP (Δm), which lead to hard p_T leptons and E_T^{miss} . The “intermediate” signal region, SR3 ℓ -I, targets the intermediate mass splittings where the mass difference between the $\tilde{\chi}_1^\pm/\tilde{\chi}_2^0$ and the $\tilde{\chi}_1^0$ are of the $O(2m_Z)$, whilst the “high-mass” region, SR3 ℓ -H targets $\Delta m > 300$ GeV. The signal region definitions are shown in Table 2.

Variable	SR3 ℓ -I	SR3 ℓ -H
lepton	$\ell^+ \ell^- \ell$	
b -tagged jet	veto	
$m_T >$	110	
m_{SFOS}	$\notin [81.2, 101.2]$	> 101.2
$p_T^{3^{\text{rd}}\ell} >$	30	80
$E_T^{\text{miss}} >$	120	60

Table 2: Table showing the signal region definitions for the three-lepton final state: the intermediate (SR3 ℓ -I) and high mass (SR3 ℓ -H) regions respectively. Units are in GeV.

7 SM Background estimation

The Standard Model backgrounds contributing in the two- and three-lepton final states can be classified into irreducible backgrounds which contain processes leading to events with prompt and isolated leptons, and reducible backgrounds, which contain events with at least one “fake” lepton. A fake lepton is a non-

prompt lepton that could originate from semi-leptonic decays of b - or c -hadrons, from misidentification of light-flavoured jets, or from photon conversions.

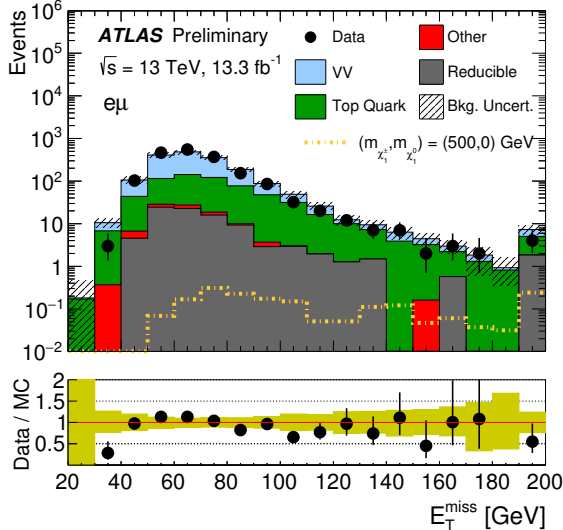
The Standard Model backgrounds entering each category are different for the two analyses. For the two-lepton analysis the dominant backgrounds are the irreducible processes $W^\pm Z \rightarrow \ell'^\pm \nu_\ell \ell^\pm \ell^-$, $ZZ \rightarrow \ell^+ \ell^- \nu_\ell \nu_\ell$ and $W^+ W^- \rightarrow \ell'^+ \nu_\ell \ell^- \bar{\nu}_\ell$ (where $\ell, \ell' = e, \mu$). MC is used to predict the kinematic distributions for these backgrounds, which are then normalised to data in two dedicated CRs that select events with either SF or DF lepton pairs. The first one (CRVV-SF) selects SF OS pairs with an invariant mass consistent with the Z -boson mass and with the same m_{T2} requirement applied as in the SR2 ℓ -A region. This region is dominated by ZZ events, with subdominant contributions from WZ and WW events. The second one (CRVV-DF) selects events with a DF OS pair and the requirement $50 < m_{T2} < 75$ GeV. This region is dominated by WW events, with a subdominant contribution from WZ events. These two CRs are then used in a simultaneous profile likelihood fit to the data that is performed using the HistFitter tool [73]. The VV backgrounds are split into events containing SF and DF leptons, and the normalisation factors of these two components are floated separately in the fit and propagated to the SRs. The CR definitions are shown in Table 3, while Figure 2 shows the E_T^{miss} and m_{T2} distributions in the CRVV-DF and CRVV-SF regions, respectively, before performing the fit. The normalisation factors extracted from the fit are 1.05 ± 0.19 for the DF processes and 1.35 ± 0.31 for the SF processes. As described further below, these normalisation factors are validated in dedicated validation regions (VRs) whose selections resemble those of the signal regions while selecting a mutually exclusive set of events. The $t\bar{t}$ contribution is estimated from simulation and validated in dedicated VRs, as discussed at the end of this section. The Z +jets and higgs boson contributions are expected to be negligible, and are estimated directly from MC.

Variable	CR VV-DF	CR VV-SF
lepton flavour	DF	SF
central light jets	0 ₃₀	0 ₂₀
central b -jets	0 ₂₀	0 ₂₀
forward jets	0 ₃₀	0 ₃₀
$ m_{\ell\ell} - m_Z $ [GeV]	—	< 10
m_{T2} [GeV]	[50, 75]	> 90

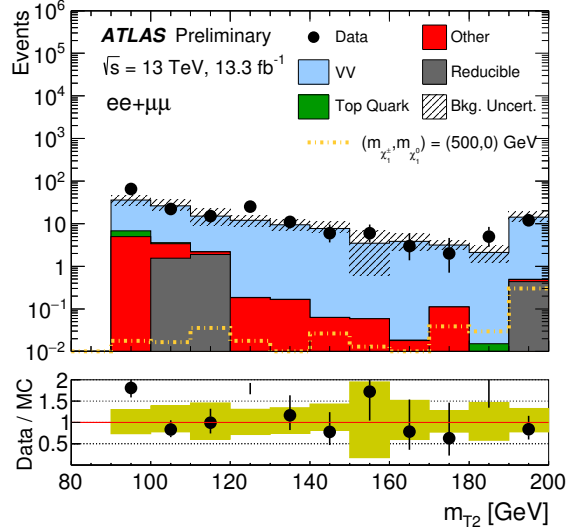
Table 3: Control region definitions for the 2L OS analysis. Units are in GeV.

The irreducible background in the three-lepton searches is mainly dominated by SM WZ diboson processes, whose prediction is estimated from MC and validated in several dedicated validation regions, each of which enhance the on-shell WZ decays, the off-shell Z contributions and the tails of the E_T^{miss} . Other background sources such as VVV , $t+V$ and Higgs processes contributing to the irreducible background of both searches are also taken from MC.

In the two-lepton channel the reducible fake lepton background arises mainly from multijet, W +jets and single top quark production, which can give one or two misidentified leptons, whereas in the three-lepton analysis the list of processes contributing to the reducible background also includes Z +jets, $t\bar{t}$, WW and in general any physics process leading to less than three prompt leptons. For both analyses the fake lepton background is estimated from data using the “matrix method” [74] (MM). This method uses two types of lepton identification criteria: “signal”, corresponding to signal leptons (as described in Section 5), and “baseline” leptons, corresponding to candidate electrons and muons. The method makes use of the number of observed events containing baseline-baseline, baseline-signal, signal-baseline and signal-signal lepton



(a) E_T^{miss} in CR-VVDF



(b) m_{T2} in CR-VVSF

Figure 2: Kinematic distributions for data, the estimated SM backgrounds, and an example SUSY scenario in the two-lepton control regions before performing the fit. The background group “Other” includes the contributions from Higgs, $Z+jets$, $V\gamma$ and VVV , while the group “Top Quark” includes the ones from Wt , $t\bar{t}$, $t\bar{t}V$.

pairs in a given SR. By measuring the probabilities for real and fake leptons passing the baseline selection criteria to also pass the signal selection, the observed event counts can be used to extract data-driven estimates for the fake-lepton background for each analysis. In the case of three leptons in the final state, the calculation is performed under the assumption that the leading lepton in the event is real which is the case for more than 90% of the studied events.

As already mentioned, the validity of the background estimation is checked in dedicated kinematical regions, mutually exclusive with respect to both the control and signal regions. The definitions of these validation regions can be found in Tables 4 and 5 for the two-lepton and three-lepton final states accordingly. The observed yields are consistent with those predicted. Figures 3 and 4 show the agreement between the background prediction and the data for distributions of kinematic variables relevant for the signal region definition for the two- and three-lepton selections respectively. Good agreement is observed.

Variable	VRVV-SF	VRVV-DF	VR-Top	VR2Lfake
lepton	$\ell^+ \ell^-$	$\ell^+ \ell^-$	$\ell^+ \ell^-$	$\ell^\pm \ell^\pm$
lepton flavour	SF	DF	DF	all
central light jets	0 ₂₀	0 ₃₀	0 ₃₀	—
central b -jets	0 ₂₀	0 ₂₀	$\geq 1_{20}$	—
forward jets	0 ₃₀	0 ₃₀	0 ₃₀	—
$ m_{\ell\ell} - m_Z $ [GeV]	> 10	—	—	> 10
m_{T2} [GeV]	[75, 90]	[75, 90]	[70, 120]	> 40

Table 4: Validation region definitions for the two-lepton analysis. Units of the subscripts of the jet numbers are in GeV.

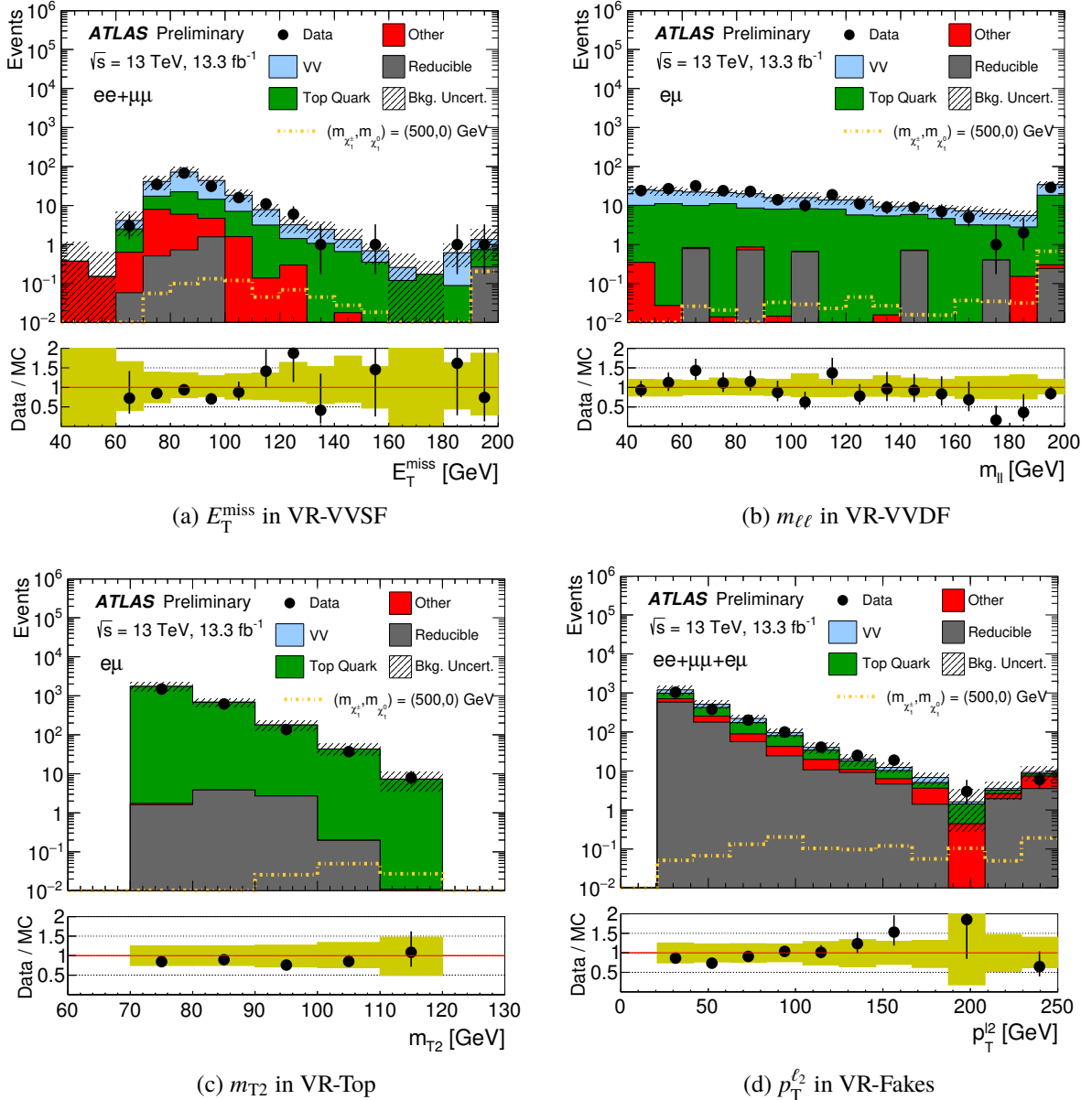


Figure 3: Kinematic distributions for data, the estimated SM backgrounds, and an example SUSY scenario in the two-lepton VRs. The background group “Other” includes the contributions from Higgs, $Z+jets$, $V\gamma$ and VVV , while the group “Top Quark” includes the ones from Wt , $t\bar{t}$, $t\bar{t}V$. The normalization factors extracted from the corresponding CRs have been applied to the $VV-SF$ and $VV-DF$ contributions. The statistical uncertainties on the background prediction are included in the uncertainty band, as well as the experimental and theoretical uncertainties.

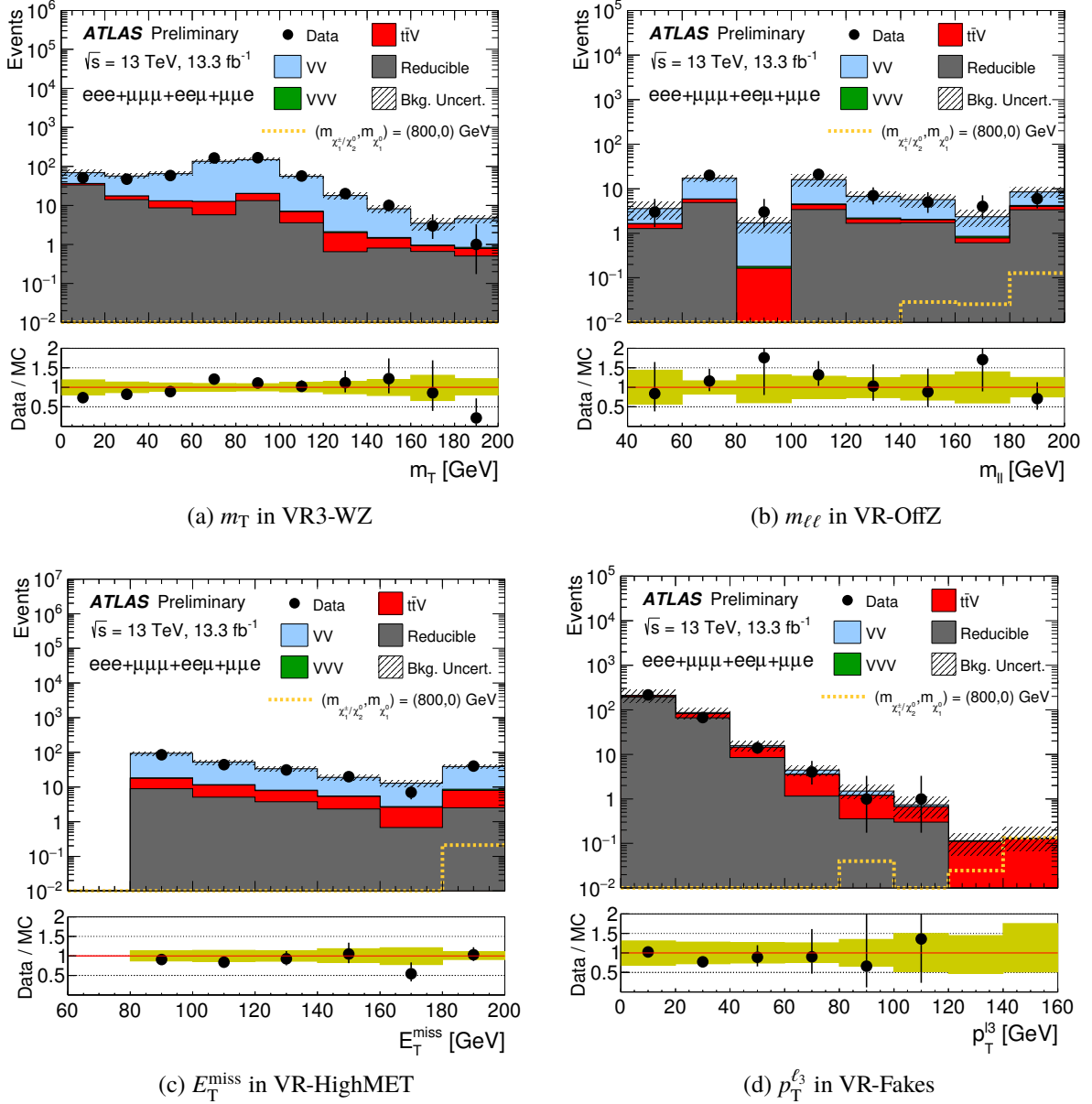


Figure 4: Kinematic distributions for data, the estimated SM backgrounds, and an example SUSY scenario in the three-lepton VRs. The statistical uncertainties on the background prediction are included in the uncertainty band, as well as the experimental and theoretical uncertainties.

Variable	VR3 ℓ WZ	VR3 ℓ highMET	VR3 ℓ offZ	VR3 ℓ fake
$N(\ell)$	3	3	3	3
p_T^{3rd} [GeV]	> 30	> 30	> 30	> 10
M_{SFOS} [GeV]	81.2–101.2	81.2–101.2	$\notin [81.2, 101.2]$	$\notin [81.2, 101.2]$
M_{III} [GeV]	$\notin [81.2, 101.2]$	$\notin [81.2, 101.2]$	$\notin [81.2, 101.2]$	$\notin [81.2, 101.2]$
$\cancel{E}_T^{\text{miss}}$ [GeV]	40–80	> 80	40–60	> 40
$N(b\text{-jets})$	–	–	–	≥ 1

Table 5: Validation region definitions in three-lepton analysis.

8 Systematic uncertainties

Several sources of experimental and theoretical systematic uncertainties are considered in the SM background estimates and signal expectations and are included in the profile likelihood fit described in Section 7. The primary sources of systematic uncertainties are related to the jet energy scale (JES) and resolution (JER), the MC modelling, the re-weighting procedure applied to simulation for matching the distribution of the average number of proton-proton interactions per bunch crossing observed in data, the systematic uncertainty considered in the non-prompt background estimation and the theoretical cross section uncertainties. The uncertainty related to the finite yields of the simulated event samples is taken into account as well. The effects of these uncertainties have been evaluated for all signal samples and background processes. In the two-lepton analysis the normalisation of the MC prediction for the dominant background processes is extracted in dedicated control regions. Therefore the systematic uncertainties only affect the extrapolation to the signal regions in these cases.

The JES and JER uncertainties are derived as a function of the p_T and η of the jet, as well as of the pileup conditions and the jet flavour composition of the selected jet sample. They are determined using a combination of simulated samples and data samples, through measurements of the jet response asymmetry in dijet, Z +jet and γ +jet events [75].

The systematic uncertainties related to the modelling of E_T^{miss} in the simulation are estimated by propagating the uncertainties on the energy and momentum scale of each of the physics objects, as well as the uncertainties on the soft term resolution and scale [69].

The remaining detector-related systematic uncertainties, such as those on lepton reconstruction efficiency, energy scale, energy resolution and on the modelling of the trigger [60, 61], have been found to be negligible.

The uncertainties coming from the background modelling in MC are estimated for dibosons by varying the renormalisation, factorisation and resummation scales used to generate the samples.

A 30% systematic uncertainty is assigned to the non-prompt lepton background estimate to account for potentially different compositions (heavy flavour, light flavour or conversions) in the signal and control regions. This uncertainty also takes into account the contamination from prompt leptons in the regions used to measure the probabilities of non-prompt leptons to pass the tight selection criteria. To take into account the pile-up dependence of the measured probabilities of mis-identifying non-prompt leptons, an additional systematic uncertainty of 15% has been considered to the MM estimation.

A summary of the leading systematic uncertainties on the total expected background for the two- and three- lepton SRs are given in Tables 6 and 7, respectively.

Systematic	SR2 ℓ A (SF)	SR2 ℓ A (DF)	SR2 ℓ B (SF)	SR2 ℓ B (DF)	SR2 ℓ C (SF)	SR2 ℓ C (DF)
Statistical uncertainty	8%	5%	9%	12%	12%	25%
Jet Energy Scale/Resolution	13-23%	12%	16-26%	3-8%	18-28%	3%
Theory	15%	21%	21%	39%	28%	66%
Reducible closure	< 1%	< 1%	< 1%	-%	< 1%	-%

Table 6: Summary of the dominant systematic uncertainties in the background estimates for each SR2 ℓ signal region as an average percentage with respect the total background. Uncertainties are quoted relative to the total expected background.

Systematic	SR3 ℓ I	SR3 ℓ H
Statistical uncertainty	18%	20%
Jet Energy Scale/Resolution	6%	6%
Theory	15%	55%
Electron Energy Scale/Resolution	2%	6%
Reducible closure	13%	--

Table 7: Summary of the dominant systematic uncertainties in the background estimates for each SR3 ℓ signal region. Uncertainties are quoted relative to the total expected background.

9 Results

As it is already mentioned in Section 7, the HistFitter framework [73], which utilises a profile-likelihood-ratio test [76], is used for the statistical interpretation of the results with the CRs and SRs both participating in the fit. The likelihood is built as the product of a Poisson probability density function describing the observed number of events in the signal region and Gaussian distributions constraining the nuisance parameters associated with the systematic uncertainties whose widths correspond to the sizes of these uncertainties; Poisson distributions are used instead for MC statistical uncertainties. Correlations of a given nuisance parameter across the different sources of backgrounds and the signal are taken into account when relevant.

To determine whether the observation is consistent with the expectation or an excess of events is present in the SRs, a background only fit has been performed first (no signal contribution has been considered), and the results are shown in Table 8 for the two-lepton analysis. Table 9 summarises the SM background expectation and observed events in the three-lepton SRs where no such fit is performed. As it can be seen the observed number of events are consistent with the background expectations within uncertainties for both the two- and three-lepton analyses. The uncertainties include both the statistical and systematic components described in Section 8.

Figure 5 shows the m_{T2} and E_T^{miss} distributions in the two-lepton signal region, SR2 ℓ A, in data together with the expected contributions from all the SM background processes with their associated total statistical and systematic uncertainties. The normalization factors extracted from the corresponding CRs are propagated to the VV-SF and VV-DF contributions. For illustration, a typical SUSY signal distribution corresponding to the most relevant benchmark scenario in each SR is displayed. Good agreement is

Region	SR2 ℓ A (SF)	SR2 ℓ A (DF)	SR2 ℓ B (SF)	SR2 ℓ B (DF)	SR2 ℓ C (SF)	SR2 ℓ C (DF)
Observed events	56	55	19	8	9	2
Fitted bkg events	70 ± 12	57.6 ± 8.5	20.7 ± 5.0	8.5 ± 3.6	10.2 ± 3.3	3.1 ± 2.3
Fitted VVSF events	56 ± 11	--	19.1 ± 5.0	--	9.5 ± 3.2	--
Fitted VVDF events	--	30.1 ± 7.9	--	7.8 ± 3.6	--	3.0 ± 2.3
Fitted Top Quark events	10.6 ± 4.0	25.1 ± 8.7	0.42 ± 0.16	0.44 ± 0.24	0.01 ± 0.00	0.01 ± 0.01
Fitted Others events	1.51 ± 0.46	0.90 ± 0.08	0.71 ± 0.29	0.23 ± 0.03	0.53 ± 0.26	0.13 ± 0.03
Fitted Reducible events	2.32 ± 0.80	1.53 ± 0.52	0.48 ± 0.17	0.00 ± 0.29	0.16 ± 0.06	0.00 ± 0.23
MC exp. SM events	56 ± 14	56 ± 12	15.8 ± 5.0	8.1 ± 3.3	7.7 ± 2.9	3.0 ± 2.1
MC exp. VVSF events	41.2 ± 10.2	--	14.2 ± 4.7	--	7.0 ± 2.8	--
MC exp. VVDF events	--	28.7 ± 6.3	--	7.4 ± 3.3	--	2.8 ± 2.1
MC exp. Top Quark events	10.6 ± 4.1	25.1 ± 8.9	0.42 ± 0.17	0.44 ± 0.24	0.01 ± 0.00	0.01 ± 0.01
MC exp. Others events	1.51 ± 0.48	0.90 ± 0.09	0.71 ± 0.30	0.23 ± 0.03	0.53 ± 0.27	0.13 ± 0.03
MC exp. Reducible events	2.32 ± 0.80	1.53 ± 0.52	0.48 ± 0.17	0.00 ± 0.29	0.16 ± 0.06	0.00 ± 0.23

Table 8: Fit results for the two-lepton signal regions, for an integrated luminosity of 13.3 fb^{-1} . The terms “Top Quark” groups contributions coming from $Wt/t\bar{t}/t\bar{t}+V$, while “Others” comprises subdominant backgrounds: VVV , Higgs, $Z+\text{jets}$ and $V+\gamma$. The errors shown are the statistical plus systematic uncertainties. Uncertainties on the fitted yields are symmetric by construction, where the negative error is truncated when reaching to zero event yield.

Region	SR3 ℓ I	SR3 ℓ H
Observed events	2	0
MC exp. SM events	4.41 ± 1.14	0.98 ± 0.50
MC exp. VV events	1.49 ± 0.45	0.69 ± 0.47
MC exp. VVV events	0.68 ± 0.36	0.20 ± 0.11
MC exp. $t\bar{t}V$ events	0.34 ± 0.11	0.09 ± 0.03
MC exp. Higgs events	0.03 ± 0.01	0.00 ± 0.00
MC exp. Reducible events	1.87 ± 0.72	0.00 ± 0.21

Table 9: Fit results for the two-lepton signal regions, for an integrated luminosity of 13.3 fb^{-1} . The errors shown are the statistical plus systematic uncertainties. Uncertainties on the fitted yields are symmetric by construction, where the negative error is truncated when reaching to zero event yield.

observed in both channels. Similarly, Figure 6 shows the m_T and E_T^{miss} kinematic distributions in the three-lepton signal regions.

In the absence of SUSY signal, exclusion limits are set on the masses of the electroweakinos for the simplified models considered in the analyses. Figure 7 shows the limits on the mass of the $\tilde{\chi}_1^0$ as a function of the $\tilde{\chi}_1^\pm$ or $\tilde{\chi}_2^0$ mass. In each case, since the signal regions are not mutually exclusive, the observed CL_s value is taken from the signal region with the best expected CL_s value, as shown in Appendix 10. These results exceed the 8 TeV limits in both searches. For the case of $\tilde{\chi}_1^+ \tilde{\chi}_1^-$ scenario the current observed limit on the $m_{\tilde{\chi}_1^\pm}$ is at 620 GeV (compared to the 480 GeV in Run I) while for the case of $\tilde{\chi}_1^\pm \tilde{\chi}_2^0$ the observed limit on the $m_{\tilde{\chi}_1^\pm / \tilde{\chi}_2^0}$ has been extended to 1 TeV for massless $\tilde{\chi}_1^0$ (compared to the 720 GeV from Run I).

Moreover, model independent upper limits have been set on the visible signal cross-section ($\langle \epsilon \sigma \rangle_{\text{obs}}^{95}$) as well as on the observed (S_{obs}^{95}) and expected (S_{exp}^{95}) events from processes beyond-the-SM. All the limits are at 95% CL. The statistical tests are performed independently for each of the signal regions after summing up the contributions from the individual final states into a single bin counting experiment. The results can be found in Table 10.

Signal Region	$\langle \epsilon \sigma \rangle_{\text{obs}}^{95} [\text{fb}]$	S_{obs}^{95}	S_{exp}^{95}	CL_B
SR2 ℓ -A	1.89	25.1	35^{+13}_{-10}	0.17
SR2 ℓ -B	1.24	16.5	$17.0^{+7.1}_{-2.8}$	0.41
SR2 ℓ -C	0.87	11.6	$12.7^{+3.0}_{-4.1}$	0.36
SR3 ℓ -I	0.28	3.7	$5.5^{+3.0}_{-1.8}$	0.16
SR3 ℓ -H	0.18	3.0	$3.4^{+2.2}_{-0.4}$	0.22

Table 10: Signal model-independent upper limits on the number of BSM events (N_{BSM}) and the visible signal cross-section ($\langle \epsilon \sigma \rangle_{\text{obs}}^{95}$) in the five SRs. Also shown are the observed and expected upper limit at 95% CL on the number of beyond-the-SM events (S_{exp}^{95} and S_{obs}^{95}) for each signal region calculated using pseudoexperiments. The $\pm 1\sigma$ variations on the expected limit due to the statistical and systematic uncertainties in the background prediction are also shown. The last column shows the CL_b value for the background-only hypothesis.

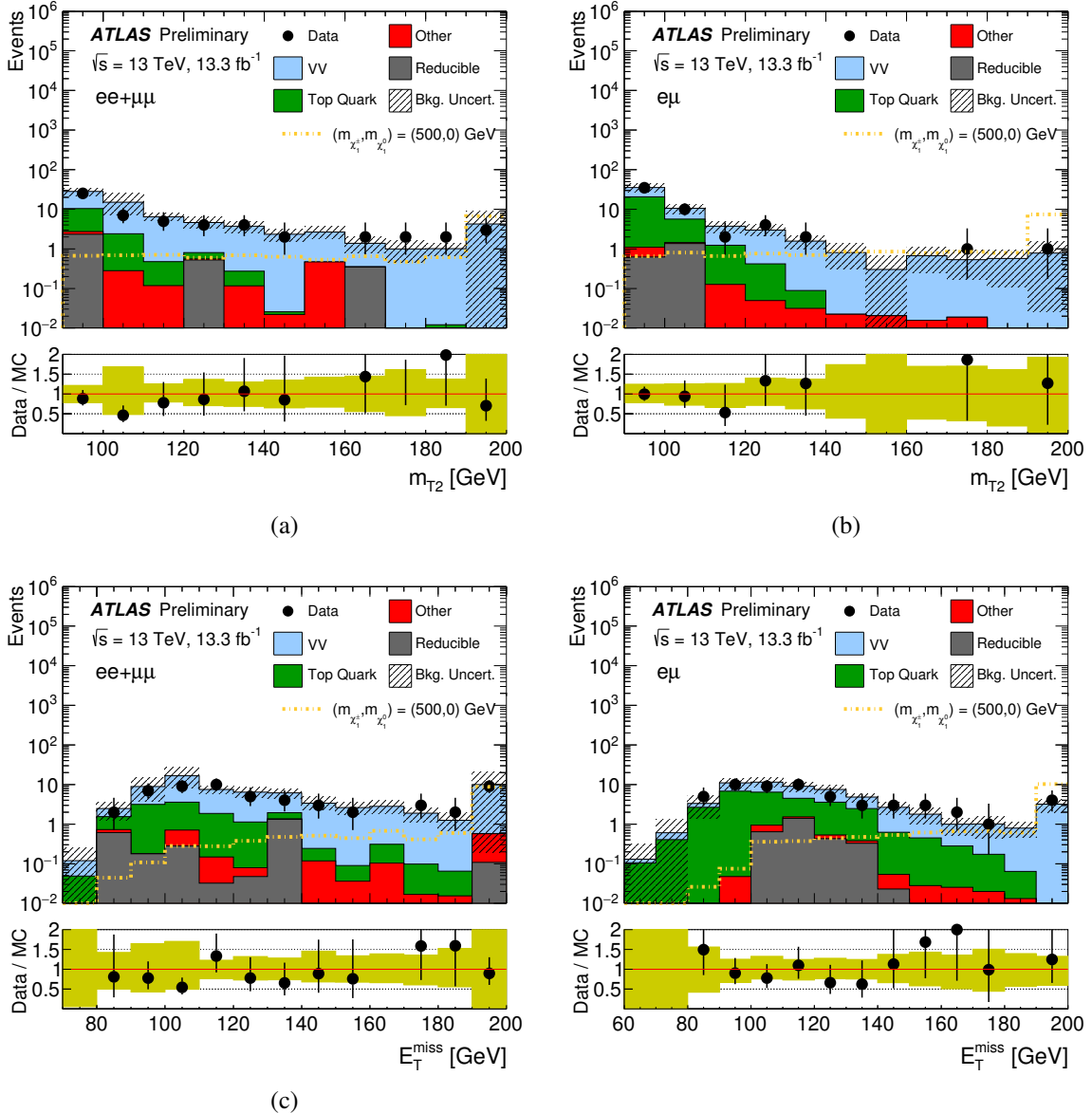


Figure 5: m_{T2} distributions for data, the estimated SM backgrounds, and an example SUSY scenario in SR2 ℓ A in the SF (a) and DF channels (b), and E_T^{miss} distributions in SR2 ℓ A in the SF (c) and DF (d) channels. The background group “Other” includes the contributions from Higgs boson production, Z -jets, $V\gamma$ and VVV , while the group “Top Quark” includes the ones from Wt , $t\bar{t}$, $t\bar{t}V$. The normalization factors extracted from the corresponding CRs are used to rescale the VV -SF and VV -DF contributions. The “Fake leptons” category corresponds to the data-driven matrix method estimate. The statistical uncertainties on the background prediction are included in the uncertainty band, as well as the experimental and theoretical uncertainties.

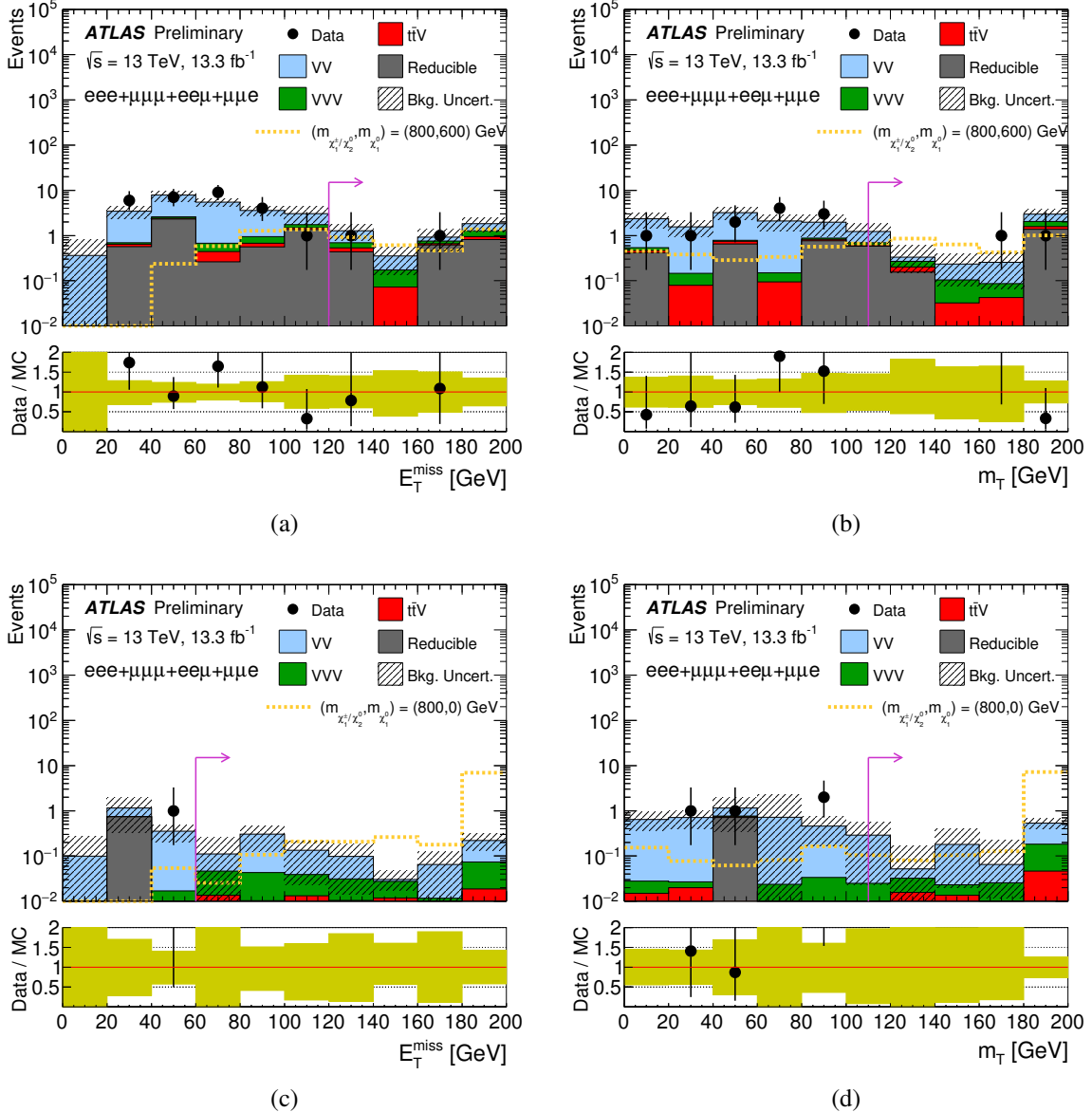


Figure 6: Distributions for data, the estimated SM backgrounds, and an example SUSY scenario for E_T^{miss} (a and c) and m_T (b and d) in SR3ℓ-I (top) and SR3ℓ-H (bottom) prior to the variable shown. The reducible components have been taken from MC and non-prompt lepton components from the Matrix Method. The arrows indicate the cut value defining the SRs. The statistical uncertainties on the background prediction are included in the uncertainty band, as well as the experimental and theoretical uncertainties.

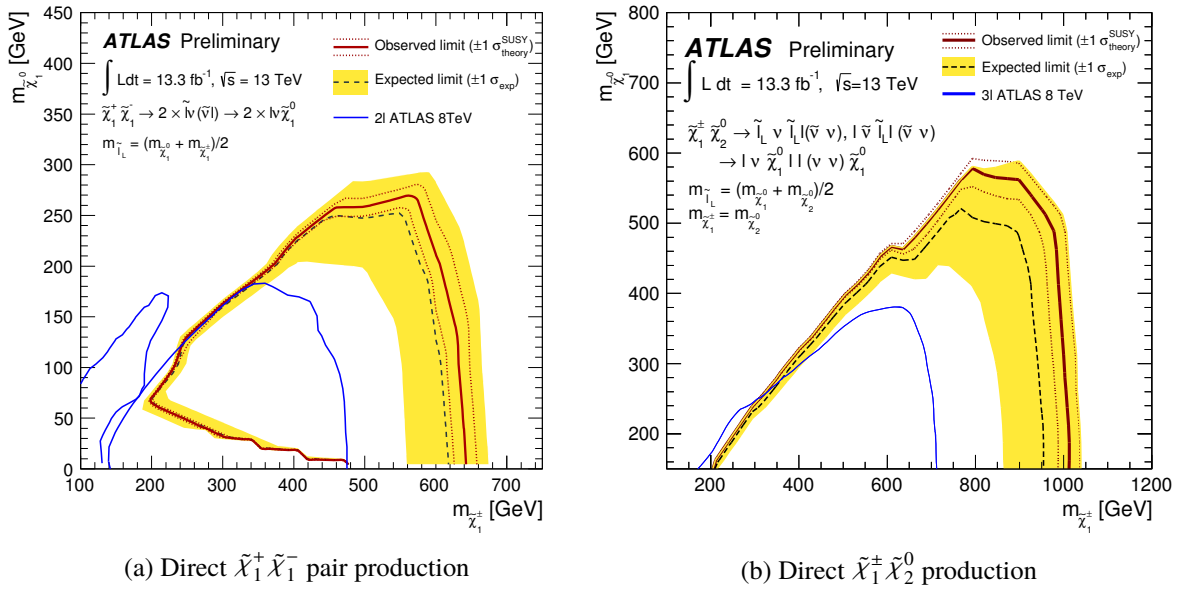


Figure 7: Observed and expected exclusion limits on the $\tilde{\chi}_2^0$, $\tilde{\chi}_1^\pm$ and $\tilde{\chi}_1^0$ masses in the context of SUSY scenarios with simplified mass spectra for direct $\tilde{\chi}_1^+ \tilde{\chi}_1^-$ pair production using the two-lepton signal regions (a) and direct $\tilde{\chi}_1^\pm \tilde{\chi}_2^0$ production using the three-lepton signal regions (b). The contours of the band around the expected limit are the $\pm 1\sigma$ results, including all uncertainties except theoretical uncertainties on the signal cross-section. The dotted lines around the observed limit illustrate the change in the observed limit as the nominal signal cross-section is scaled up and down by the theoretical uncertainty. All limits are computed at 95% CL. The observed limits obtained from ATLAS during LHC Run I are also shown [19–21].

10 Conclusion

A search for the electroweak production of supersymmetric particles in events with exactly two- and three-leptons and E_T^{miss} is presented. The analysis is performed with proton-proton collision data at $\sqrt{s} = 13$ TeV collected with the ATLAS detector at the Large Hadron Collider corresponding to an integrated luminosity of 13.3 fb^{-1} . With no significant excess over the Standard Model expectation observed, results are interpreted in the framework of simplified models featuring chargino and neutralino production. The limits set by this search extend the previous ones set during the LHC Run I by 140 GeV for the $\tilde{\chi}_1^+ \tilde{\chi}_1^-$ production and by 300 GeV for the case of $\tilde{\chi}_1^\pm \tilde{\chi}_2^0$ production.

Appendix

In each final state, since the signal regions are not orthogonal, the observed CL_s value is taken from the signal region with the best expected CL_s value, the selection used for the results reported in Figure 7 is shown in Figure 8.

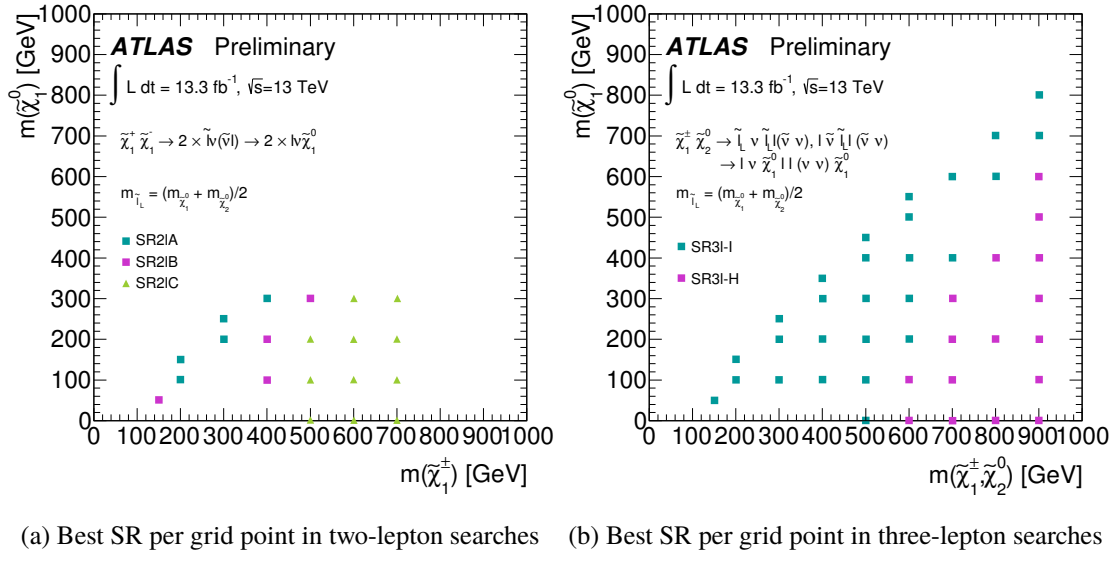


Figure 8: The SR used for each signal point is shown in (a) and (b) for the two- and three-lepton searches respectively.

References

- [1] Yu. A. Golfand and E. P. Likhtman, *Extension of the Algebra of Poincare Group Generators and Violation of P Invariance*, JETP Lett. **13** (1971) 323, [Pisma Zh. Eksp. Teor. Fiz. 13, 452 (1971)].
- [2] D. V. Volkov and V. P. Akulov, *Is the Neutrino a Goldstone Particle?*, Phys. Lett. B **46** (1973) 109.
- [3] J. Wess and B. Zumino, *Supergauge Transformations in Four-Dimensions*, Nucl. Phys. B **70** (1974) 39.
- [4] J. Wess and B. Zumino, *Supergauge Invariant Extension of Quantum Electrodynamics*, Nucl. Phys. B **78** (1974) 1.
- [5] S. Ferrara and B. Zumino, *Supergauge Invariant Yang-Mills Theories*, Nucl. Phys. B **79** (1974) 413.
- [6] A. Salam and J. A. Strathdee, *Supersymmetry and Nonabelian Gauges*, Phys. Lett. B **51** (1974) 353.
- [7] S. P. Martin, *A Supersymmetry primer*, (1997), [Adv. Ser. Direct. High Energy Phys. 18, 1 (1998)], arXiv: [hep-ph/9709356 \[hep-ph\]](https://arxiv.org/abs/hep-ph/9709356).

- [8] N. Sakai, *Naturalness in Supersymmetric Guts*, *Z. Phys. C* **11** (1981) 153.
- [9] S. Dimopoulos, S. Raby and F. Wilczek, *Supersymmetry and the Scale of Unification*, *Phys. Rev. D* **24** (1981) 1681.
- [10] L. E. Ibanez and G. G. Ross, *Low-Energy Predictions in Supersymmetric Grand Unified Theories*, *Phys. Lett. B* **105** (1981) 439.
- [11] S. Dimopoulos and H. Georgi, *Softly Broken Supersymmetry and SU(5)*, *Nucl. Phys. B* **193** (1981) 150.
- [12] P. Fayet, *Supersymmetry and Weak, Electromagnetic and Strong Interactions*, *Phys. Lett. B* **64** (1976) 159.
- [13] P. Fayet, *Spontaneously Broken Supersymmetric Theories of Weak, Electromagnetic and Strong Interactions*, *Phys. Lett. B* **69** (1977) 489.
- [14] G. R. Farrar and P. Fayet, *Phenomenology of the Production, Decay, and Detection of New Hadronic States Associated with Supersymmetry*, *Phys. Lett. B* **76** (1978) 575.
- [15] H. Goldberg, *Constraint on the Photino Mass from Cosmology*, *Phys. Rev. Lett.* **50** (1983) 1419, [Erratum: *Phys. Rev. Lett.* 103, 099905 (2009)].
- [16] J. R. Ellis et al., *Supersymmetric Relics from the Big Bang*, *Nucl. Phys. B* **238** (1984) 453.
- [17] ATLAS Collaboration, ‘Further searches for squarks and gluinos in final states with jets and missing transverse momentum at $\sqrt{s} = 13$ TeV with the ATLAS detector’, tech. rep. ATLAS-CONF-2016-078, CERN, 2016, URL: <https://cds.cern.ch/record/2206252>.
- [18] CMS Collaboration, *Search for supersymmetry in the multijet and missing transverse momentum final state in pp collisions at 13 TeV*, *Phys. Lett. B* **758** (2016) 152, arXiv: [1602.06581 \[hep-ex\]](https://arxiv.org/abs/1602.06581).
- [19] ATLAS collaboration, *Search for the direct production of charginos, neutralinos and staus in final states with at least two hadronically decaying taus and missing transverse momentum in pp collisions at $\sqrt{s} = 8$ TeV with the ATLAS detector*, *JHEP* **10** (2014) 096, arXiv: [1407.0350 \[hep-ex\]](https://arxiv.org/abs/1407.0350).
- [20] ATLAS collaboration, *Search for direct production of charginos and neutralinos in events with three leptons and missing transverse momentum in $\sqrt{s} = 8$ TeV pp collisions with the ATLAS detector*, *JHEP* **04** (2014) 169, arXiv: [1402.7029 \[hep-ex\]](https://arxiv.org/abs/1402.7029).
- [21] ATLAS collaboration, *Search for the electroweak production of supersymmetric particles in $\sqrt{s}=8$ TeV pp collisions with the ATLAS detector*, *Phys. Rev. D* **93** (2016) 052002, arXiv: [1509.07152 \[hep-ex\]](https://arxiv.org/abs/1509.07152).
- [22] CMS Collaboration, *Searches for electroweak neutralino and chargino production in channels with Higgs, Z, and W bosons in pp collisions at 8 TeV*, *Phys. Rev. D* **90** (2014) 092007, arXiv: [1409.3168 \[hep-ex\]](https://arxiv.org/abs/1409.3168).
- [23] CMS collaboration, *Searches for electroweak production of charginos, neutralinos, and sleptons decaying to leptons and W, Z, and Higgs bosons in pp collisions at 8 TeV*, *Eur. Phys. J. C* **74** (2014) 3036, arXiv: [1405.7570 \[hep-ex\]](https://arxiv.org/abs/1405.7570).
- [24] ATLAS Collaboration, *The ATLAS Experiment at the CERN Large Hadron Collider*, *JINST* **3** (2008) S08003.

[25] ATLAS Collaboration, *ATLAS Insertable B-Layer Technical Design Report*, CERN-LHCC-2010-013. ATLAS-TDR-19, 2010, URL: <http://cds.cern.ch/record/1291633>.

[26] J. Alwall et al., *Simplified Models for a First Characterization of New Physics at the LHC*, *Phys. Rev. D* **79** (2009) 075020, arXiv: [0810.3921 \[hep-ph\]](#).

[27] ATLAS Collaboration, *Improved luminosity determination in pp collisions at $\sqrt{s} = 7$ TeV using the ATLAS detector at the LHC*, *Eur. Phys. J. C* **73** (2013) 2518, arXiv: [1302.4393 \[hep-ex\]](#).

[28] ATLAS Collaboration, *Luminosity determination in pp collisions at $\sqrt{s} = 8$ TeV using the ATLAS detector at the LHC*, to be submitted to *Eur. Phys. J. C*.

[29] ATLAS Collaboration, *The ATLAS Simulation Infrastructure*, *Eur. Phys. J. C* **70** (2010) 823, arXiv: [1005.4568 \[hep-ex\]](#).

[30] S. Agostinelli et al., *GEANT4: A Simulation toolkit*, *Nucl.Instrum.Meth. A* **506** (2003) 250.

[31] ATLAS Collaboration, *The simulation principle and performance of the ATLAS fast calorimeter simulation FastCaloSim*, ATL-PHYS-PUB-2010-013, 2010, URL: <http://cds.cern.ch/record/1300517>.

[32] T. Gleisberg et al., *Event generation with SHERPA 1.1*, *JHEP* **02** (2009) 007, arXiv: [0811.4622 \[hep-ph\]](#).

[33] ATLAS Collaboration, *Multi-boson simulation for 13 TeV ATLAS analyses*, ATL-PHYS-PUB-2016-002, 2016, URL: <http://cdsweb.cern.ch/record/2119986>.

[34] T. Gleisberg and S. Höche, *Comix, a new matrix element generator*, *JHEP* **12** (2008) 039, arXiv: [0808.3674 \[hep-ph\]](#).

[35] F. Caccioli, P. Maierhofer and S. Pozzorini, *Scattering Amplitudes with Open Loops*, *Phys. Rev. Lett.* **108** (2012) 111601, arXiv: [1111.5206 \[hep-ph\]](#).

[36] S. Schumann and F. Krauss, *A Parton shower algorithm based on Catani-Seymour dipole factorisation*, *JHEP* **03** (2008) 038, arXiv: [0709.1027 \[hep-ph\]](#).

[37] S. Höche et al., *QCD matrix elements + parton showers: The NLO case*, *JHEP* **04** (2013) 027, arXiv: [1207.5030 \[hep-ph\]](#).

[38] H.-L. Lai et al., *New parton distributions for collider physics*, *Phys. Rev. D* **82** (2010) 074024, arXiv: [1007.2241 \[hep-ph\]](#).

[39] ATLAS Collaboration, *Monte Carlo Generators for the Production of a W or Z/γ^* Boson in Association with Jets at ATLAS in Run 2*, ATL-PHYS-PUB-2016-003, 2016, URL: <http://cdsweb.cern.ch/record/2120133>.

[40] ATLAS Collaboration, *Simulation of top-quark production for the ATLAS experiment at $\sqrt{s} = 13$ TeV*, ATL-PHYS-PUB-2016-004, 2016, URL: <http://cdsweb.cern.ch/record/2120417>.

[41] M. Czakon and A. Mitov, *Top++: A Program for the Calculation of the Top-Pair Cross-Section at Hadron Colliders*, *Comput.Phys.Commun.* **185** (2014) 2930, arXiv: [1112.5675 \[hep-ph\]](#).

[42] J. Alwall et al., *MadGraph 5 : Going Beyond*, *JHEP* **06** (2011) 128, arXiv: [1106.0522 \[hep-ph\]](#).

[43] T. Sjöstrand, S. Mrenna and P. Z. Skands, *A Brief Introduction to PYTHIA 8.1*, *Comput. Phys. Commun.* **178** (2008) 852, arXiv: [0710.3820 \[hep-ph\]](#).

[44] ATLAS Collaboration, *Modelling of the $t\bar{t}H$ and $t\bar{t}V$ ($V = W, Z$) processes for $\sqrt{s} = 13$ TeV ATLAS analyses*, ATL-PHYS-PUB-2015-022, 2016, URL: <http://cds.cern.ch/record/2120826>.

[45] ATLAS Collaboration, *ATLAS Pythia8 tunes to 7 TeV data*, ATL-PHYS-PUB-2014-021, 2014, URL: <http://cds.cern.ch/record/1966419>.

[46] R. D. Ball et al., *Parton distributions with LHC data*, *Nucl. Phys.* **B867** (2013) 244, arXiv: [1207.1303 \[hep-ph\]](#).

[47] J. Alwall et al., *The automated computation of tree-level and next-to-leading order differential cross sections, and their matching to parton shower simulations*, *JHEP* **07** (2014) 079, arXiv: [1405.0301 \[hep-ph\]](#).

[48] L. Lönnblad and S. Prestel, *Matching Tree-Level Matrix Elements with Interleaved Showers*, *JHEP* **03** (2012) 019, arXiv: [1109.4829 \[hep-ph\]](#).

[49] W. Beenakker et al., *Squark and gluino production at hadron colliders*, *Nucl. Phys. B* **492** (1997) 51, arXiv: [hep-ph/9610490](#).

[50] A. Kulesza and L. Motyka, *Threshold resummation for squark-antisquark and gluino-pair production at the LHC*, *Phys. Rev. Lett.* **102** (2009) 111802, arXiv: [0807.2405 \[hep-ph\]](#).

[51] A. Kulesza and L. Motyka, *Soft gluon resummation for the production of gluino-gluino and squark-antisquark pairs at the LHC*, *Phys. Rev. D* **80** (2009) 095004, arXiv: [0905.4749 \[hep-ph\]](#).

[52] W. Beenakker et al., *Soft-gluon resummation for squark and gluino hadroproduction*, *JHEP* **0912** (2009) 041, arXiv: [0909.4418 \[hep-ph\]](#).

[53] W. Beenakker et al., *Squark and gluino hadroproduction*, *Int. J. Mod. Phys. A* **26** (2011) 2637, arXiv: [1105.1110 \[hep-ph\]](#).

[54] M. Krämer et al., *Supersymmetry production cross sections in pp collisions at $\sqrt{s} = 7$ TeV*, (2012), arXiv: [1206.2892 \[hep-ph\]](#).

[55] D. J. Lange, *The EvtGen particle decay simulation package*, *Nucl. Instrum. Meth.* **A462** (2001) 152.

[56] ATLAS Collaboration, *Summary of ATLAS Pythia 8 tunes*, ATL-PHYS-PUB-2012-003, 2012, URL: <http://cdsweb.cern.ch/record/1474107>.

[57] A. D. Martin et al., *Parton distributions for the LHC*, *Eur. Phys. J.* **C63** (2009) 189, arXiv: [0901.0002 \[hep-ph\]](#).

[58] ATLAS Collaboration, *Vertex Reconstruction Performance of the ATLAS Detector at $\sqrt{s} = 13$ TeV*, ATL-PHYS-PUB-2015-026, 2015, URL: <http://cdsweb.cern.ch/record/2037717>.

[59] ATLAS Collaboration, *Electron efficiency measurements with the ATLAS detector using the 2012 LHC proton-proton collision data*, ATL-CONF-2014-032, 2014, URL: <http://cds.cern.ch/record/1706245>.

[60] ATLAS Collaboration, *Electron identification measurements in ATLAS using $\sqrt{s} = 13$ TeV data with 50 ns bunch spacing*, ATL-PHYS-PUB-2015-041, 2015, URL: <http://cds.cern.ch/record/2048202>.

[61] ATLAS Collaboration, *Muon reconstruction performance in early Run II*, ATL-PHYS-PUB-2015-037, 2015, URL: <http://cds.cern.ch/record/2047831>.

[62] M. Cacciari, G. P. Salam and G. Soyez, *The anti- k_T jet clustering algorithm*, *JHEP* **04** (2008) 063, arXiv: [0802.1189 \[hep-ph\]](https://arxiv.org/abs/0802.1189).

[63] W. Lampl et al., *Calorimeter Clustering Algorithms: Description and Performance*, ATL-LARG-PUB-2008-002, 2008, URL: <http://cdsweb.cern.ch/record/1099735>.

[64] ATLAS Collaboration, *Jet Calibration and Systematic Uncertainties for Jets Reconstructed in the ATLAS Detector at $\sqrt{s} = 13$ TeV*, ATL-PHYS-PUB-2015-015, 2015, URL: <http://cds.cern.ch/record/2028594>.

[65] ATLAS Collaboration, *Tagging and suppression of pileup jets with the ATLAS detector*, ATLAS-CONF-2014-018, 2014, URL: <http://cdsweb.cern.ch/record/1700870>.

[66] ATLAS Collaboration, *Optimization of the ATLAS b-tagging performance for the 2016 LHC Run*, ATL-PHYS-PUB-2016-012, 2016, URL: <http://cds.cern.ch/record/2160731>.

[67] ATLAS Collaboration, *Performance of b-Jet Identification in the ATLAS Experiment*, *JINST* **11** (2016) P04008, arXiv: [1512.01094 \[hep-ex\]](https://arxiv.org/abs/1512.01094).

[68] ATLAS Collaboration, *Performance of missing transverse momentum reconstruction for the ATLAS detector in the first proton-proton collisions at $\sqrt{s} = 13$ TeV*, ATL-PHYS-PUB-2015-027, 2015, URL: <http://cds.cern.ch/record/2037904>.

[69] ATLAS Collaboration, *Expected performance of missing transverse momentum reconstruction for the ATLAS detector at $\sqrt{s} = 13$ TeV*, ATL-PHYS-PUB-2015-023, 2015, URL: <http://cds.cern.ch/record/2037700>.

[70] ATLAS Collaboration, *Data-Quality Requirements and Event Cleaning for Jets and Missing Transverse Energy Reconstruction with the ATLAS Detector in Proton-Proton Collisions at a Center-of-Mass Energy of $\sqrt{s} = 7$ TeV*, ATLAS-CONF-2010-038, 2010, URL: <http://cdsweb.cern.ch/record/1277678>.

[71] C. Lester and D. Summers, *Measuring masses of semiinvisibly decaying particles pair produced at hadron colliders*, *Phys.Lett.* **B463** (1999) 99, arXiv: [hep-ph/9906349 \[hep-ph\]](https://arxiv.org/abs/hep-ph/9906349).

[72] A. Barr, C. Lester and P. Stephens, *$m(T2)$: The Truth behind the glamour*, *J.Phys.* **G29** (2003) 2343, arXiv: [hep-ph/0304226 \[hep-ph\]](https://arxiv.org/abs/hep-ph/0304226).

[73] M. Baak et al., *HistFitter software framework for statistical data analysis*, *Eur.Phys.J.* **C75** (2015) 153, arXiv: [1410.1280 \[hep-ex\]](https://arxiv.org/abs/1410.1280).

[74] ATLAS Collaboration, *Measurement of the top quark-pair production cross section with ATLAS in pp collisions at $\sqrt{s} = 7$ TeV*, *The European Physical Journal C* **71** (3 2011) 1, ISSN: 1434-6044, URL: <http://dx.doi.org/10.1140/epjc/s10052-011-1577-6>.

[75] ATLAS Collaboration, *Jet Calibration and Systematic Uncertainties for Jets Reconstructed in the ATLAS Detector at $\sqrt{s} = 13$ TeV*, ATL-PHYS-PUB-2015-015, 2015, URL: <https://cds.cern.ch/record/2037613>.

[76] G. Cowan et al., *Asymptotic formulae for likelihood-based tests of new physics*, *Eur. Phys. J.* **C71** (2011) 1554, [Erratum: *Eur. Phys. J.* **C73** (2013) 2501], arXiv: [1007.1727 \[physics.data-an\]](https://arxiv.org/abs/1007.1727).